



# SARAS 2 Constraints on Global 21 cm Signals from the Epoch of Reionization

Saurabh Singh<sup>1</sup>, Ravi Subrahmanyan<sup>1</sup>, N. Udaya Shankar<sup>1</sup>, Mayuri Sathyanarayana Rao<sup>1</sup>, Anastasia Fialkov<sup>2</sup>,  
Aviad Cohen<sup>3</sup>, Rennan Barkana<sup>3</sup>, B. S. Girish<sup>1</sup>, A. Raghunathan<sup>1</sup>, R. Somashekar<sup>1</sup>, and K. S. Srivani<sup>1</sup>

<sup>1</sup>Raman Research Institute, C V Raman Avenue, Sadashivanagar, Bangalore 560080, India; [saurabhs@rri.res.in](mailto:saurabhs@rri.res.in)

<sup>2</sup>Harvard-Smithsonian Center for Astrophysics, Institute for Theory and Computation, 60 Garden Street, Cambridge, MA 02138, USA

<sup>3</sup>Raymond and Beverly Sackler School of Physics and Astronomy, Tel Aviv University, Tel Aviv 69978, Israel

Received 2017 November 30; revised 2018 February 28; accepted 2018 March 28; published 2018 May 4

## Abstract

Spectral distortions in the cosmic microwave background over the 40–200 MHz band are imprinted by neutral hydrogen in the intergalactic medium prior to the end of reionization. This signal, produced in the redshift range  $z = 6\text{--}34$  at the rest-frame wavelength of 21 cm, has not been detected yet; and a poor understanding of high-redshift astrophysics results in a large uncertainty in the expected spectrum. The SARAS 2 radiometer was purposely designed to detect the sky-averaged 21 cm signal. The instrument, deployed at the Timbaktu Collective (Southern India) in 2017 April–June, collected 63 hr of science data, which were examined for the presence of the cosmological 21 cm signal. In our previous work, the first-light data from the SARAS 2 radiometer were analyzed with Bayesian likelihood-ratio tests using 264 plausible astrophysical scenarios. In this paper we reexamine the data using an improved analysis based on the frequentist approach and forward-modeling. We show that SARAS 2 data reject 20 models, out of which 15 are rejected at a significance  $>5\sigma$ . All the rejected models share the scenario of inefficient heating of the primordial gas by the first population of X-ray sources, along with rapid reionization.

*Key words:* cosmic background radiation – cosmology: observations – dark ages, reionization, first stars – methods: observational

## 1. Introduction

The Universe at the epochs of Cosmic Dawn (CD) and Reionization (EoR) is poorly constrained by observations, which results in a large scatter in theoretical predictions for galaxy and star formation. One of the most powerful potential probes of these eras is the rest-frame 21 cm signal of neutral hydrogen (HI) produced by the intergalactic medium (IGM) prior to the end of the EoR at  $z \sim 6$ . The intensity of this signal is tied to the star formation history and to the ionization and thermal histories of the IGM (Barkana 2016). Hence, its measurement will bracket astrophysical properties of the first UV and X-ray sources, including the ionizing efficiency of first stars and quasars, the luminosity and spectra of the first population of black holes, and the properties of dark matter particles (Furlanetto 2006; Pritchard & Loeb 2010; Mirocha et al. 2013, 2015; Evoli et al. 2014; Fialkov et al. 2014; Sitwell et al. 2014; Cohen et al. 2017; Mirocha et al. 2017). At present, these properties are poorly understood, allowing for a large variety of plausible 21 cm spectra (Cohen et al. 2017).

The main feature of the sky-averaged (a.k.a. global) 21 cm spectrum observed against the cosmic microwave background (CMB) is the deep absorption trough that traces the adiabatic cooling of the IGM and its subsequent heating by the first X-ray sources (X-ray binaries and black holes). The thermal history is imprinted in the 21 cm signal owing to the Wouthuysen-Field effect (Wouthuysen 1952; Field 1958): the 21 cm transition is coupled to the temperature of the gas by the stellar Ly $\alpha$  photons. The strength of the coupling depends on the intensity of the Ly $\alpha$  background and is correlated with the process of star formation itself. When the population of X-ray sources builds up, producing a sufficient amount of photons with energy in the  $\sim 0.1\text{--}3$  keV range, the temperature

of the IGM rises, leading to a reduction in the 21 cm intensity and shaping the absorption trough. Considering  $\sim 200$  different plausible astrophysical scenarios, Cohen et al. (2017) showed that, owing to the uncertainty in the high-redshift astrophysics, the depth of the absorption trough can vary between  $-25$  and  $-240$  mK and its central frequency can be anywhere between  $40 < \nu < 120$  MHz (corresponding to  $z \sim 11\text{--}34$ ). Localization of this feature will directly constrain the intensity of the Ly $\alpha$  background and the cosmic heating rate.

At lower redshifts  $z \sim 6\text{--}11$  (higher frequencies  $\sim 120\text{--}200$  MHz) reionization by stars and quasars is ongoing, and the intensity of the 21 cm signal decreases, owing to the lesser fraction of HI in the IGM. As more free parameters are added to the modeling (e.g., ionizing efficiency of sources and mean free path of the ionizing photons), the expected signal is even less constrained. In particular, its shape depends on the balance between the heating and ionization rates: if heating occurs faster than ionization, the signal will be seen in emission during the EoR, otherwise it will be seen in absorption at any epoch. If it is present, the emission feature can be as strong as 32 mK, peaking between 80 and 160 MHz. Detecting the EoR signal will allow constraint of the X-ray heating efficiency together with the ionization efficiency of sources (Cohen et al. 2017); it will also measure the CMB optical depth  $\tau$  at much higher precision than what can be done with the CMB (Fialkov & Loeb 2016; Liu et al. 2016).

Ongoing experiments that target detection of the global 21 cm signal from CD and EoR are plagued by orders of magnitude stronger Galactic and extragalactic foregrounds (Shaver et al. 1999; Sathyanarayana Rao et al. 2017b). These foregrounds couple to the radiometer system through its frequency-dependent transfer function and can potentially confuse a detection of the relatively faint cosmological 21 cm signal. Additional challenges include modeling the internal additives from within the receiver system, which are often

<sup>\*</sup> Joint Astronomy Program, Indian Institute of Science, Bangalore 560012, India.

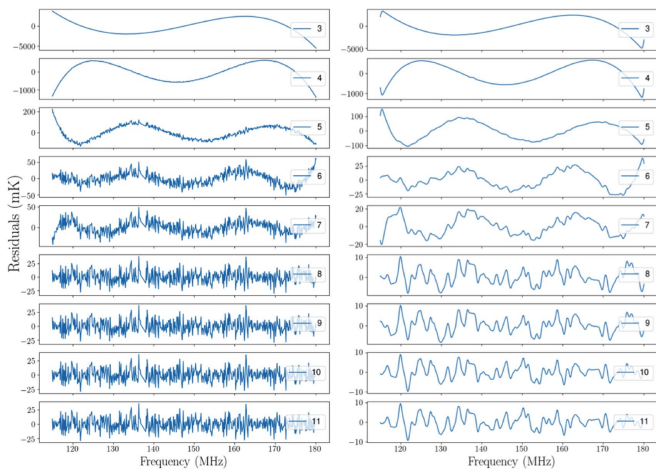


**Figure 1.** Data residuals obtained after subtracting different orders of polynomials; the numbers in the legends indicate the number of terms in the polynomial fit. The panel on the left shows the residuals without any averaging in frequency, while the panel on the right shows the residuals smoothed at the 1 MHz scale using a Hanning window (Oppenheim 1999).

difficult to calibrate, and excision of terrestrial radio frequency interference (RFI). All these demand stringent requirements on the antenna and receiver design, clever calibration strategies, and innovative data analysis methods (Singh et al. 2018).

Despite the challenges, pioneering experiments have attained sensitivity levels at which plausible scenarios of reionization are being ruled out. The first constraint on EoR from global 21 cm experiments came from the Experiment to Detect the Global EoR Signature (EDGES) high-band antenna covering the 90–190 MHz frequency range, which ruled out rapid reionization with  $\Delta z < 0.06$  at the 95% confidence level (Bowman & Rogers 2010). Bernardi et al. (2016) used an outrigger Large Aperture Experiment to Detect the Dark Ages (LEDA) antenna to measure the spectrum at lower frequencies, 50–100 MHz. This measurement constrained the amplitude of the absorption trough to be less than 890 mK for a Gaussian-shaped absorption with a width greater than 6.5 MHz at the 95% confidence level. Constraints on the redshift interval,  $\Delta z$ , over which reionization occurred, have significantly improved with the recent high-band data from EDGES (Monsalve et al. 2017). The constraint depends on the assumptions for the thermal state of the IGM during the EoR: for heated IGM models, the duration shorter than  $\Delta z \approx 1$  with EoR occurring at  $z \approx 8.5$  is rejected with 95% confidence; whereas for cold IGM scenarios,  $\Delta z \lesssim 2$  is rejected over most of the plausible redshift range for the EoR. All the analyses mentioned above were carried out with the adoption of simple functions to mimic the cosmological signal: a  $\tanh$  form was used to imitate the variation in ionization fraction with frequency, and the absorption trough was modeled as a Gaussian.

Realistic global 21 cm signals (part of which were published in Cohen et al. 2017) were used for the first time in the analysis of the first-light data of Shaped Antenna measurement of the background RADIO SPECTRUM 2 (SARAS 2) radiometer (Singh et al. 2017). The spectra are outputs of a self-consistent 4-D (3 spatial dimensions + time) large-scale simulation of the high-redshift universe (e.g., Visbal et al. 2012; Fialkov & Barkana 2014). In this simulation X-ray and UV photons emitted by a realistic non-uniform and time-dependent population of sources are propagated accounting for time delay and cosmological redshift. These photons heat and ionize the

initially cold and neutral IGM, which produces the 21 cm signal. Using Bayesian likelihood-ratio tests the SARAS 2 data were shown to disfavor 9 out of 264 different astrophysical scenarios with  $1\sigma$  confidence over the rejected set. All these models share late IGM heating along with rapid reionization (Singh et al. 2017a).

In this paper we employ improved statistical techniques to analyze the same data of SARAS 2 and use the same set of astrophysical models as in Singh et al. (2017a). We adopt the frequentist approach of Monsalve et al. (2017), including forward-modeling, and revisit the likelihoods for each one of the cosmological signals. The paper is organized as follows. Section 2 summarizes the SARAS 2 system and the observations. Section 3 outlines the data analysis method. In Section 4 we discuss astrophysical constraints. We discuss limitations of the analysis methods in Section 5. We conclude in Section 6.

## 2. SARAS 2: A Description of the Radiometer and Observations

SARAS 2 is a precision radiometer, custom designed to detect the global 21 cm signal from CD and EoR, covering the band 40–200 MHz, which corresponds to the redshift range  $z \sim 6$ –34. SARAS 2 has been designed to have (i) a telescope beam that is frequency-independent so that structure in the foreground sky brightness does not result in any spectral shapes in the response (Singh et al. 2017b, Section 3.2.1), and (ii) a receiver transfer function and internal systematics—both multiplicative and additive—that are spectrally smooth to allow a separation of foregrounds and systematics from the predicted global cosmological 21 cm signals (Singh et al. 2017b, Section 7).

The system was deployed at a relatively radio quiet-site at the Timbaktu Collective in Southern India during 2017 April–June. The data were processed to reject RFI, calibrate the receiver gain and bandpass, and the data along with the GMOSS model (Sathyanarayana Rao et al. 2017a) for the radio sky were used to derive the total efficiency of the radiometer. A total of 63 hr of useful night time data were obtained over the frequency band of 110–200 MHz. Data residuals, after modeling for foregrounds and internal systematics, yielded spectra with resolution of 122 kHz and root-mean-square (rms) noise of 11 mK, consistent with expectations from the radiometer system temperature, observing time, etc.

We show in Figure 1 the data residuals for 63-hr averaging for polynomial fits with different number of terms. With increasing orders, the residuals approach thermal noise levels, going down to thermal noise for an 8-term polynomial fit. We do not see any evidence of systematics. We also show the residuals across the nights in Figure 2 for the 8-term polynomial fit, which are also consistent with noise.

## 3. Signal Extraction: A Frequentist Approach

In our first paper (Singh et al. 2017a) we used Bayesian likelihood-ratio tests to verify whether or not each one of the theoretical signals is consistent with the first-light data. Here, we use the same data and the same set of models, but a different statistical approach.

### 3.1. Foreground Modeling

The observed data consists of the cosmological and foreground signals, propagated through the SARAS 2 system,

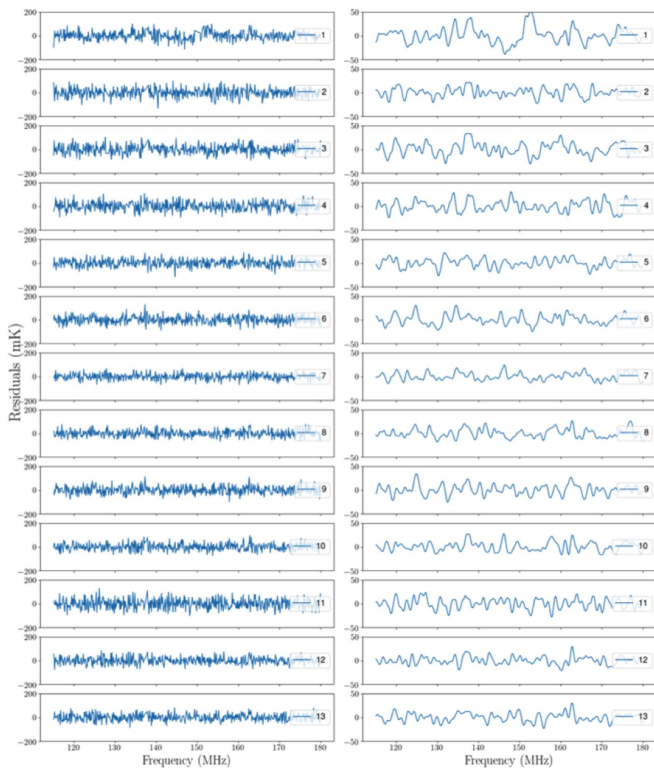


**Figure 2.** Residuals from each night selected for analysis, obtained by fitting an 8-term polynomial. On average, the observing time for a single night is  $\sim 5$  hr. The rms noise for each night is close to 33 mK. The total observing time is 63 hr for 13 nights. The panel on the right shows the residual from each night after averaging in frequency at the 1 MHz scale using a Hanning window (Oppenheim 1999). The numbers in the legend represent indices for different nights.

plus the internal systematics generated by the instrument. Both the foreground and the systematics are modeled using polynomials over an optimal frequency band (as described in Section 3.3). The total contribution of foregrounds and systematics is thus  $F(\nu) = \sum_{i=0}^{N-1} c_i \nu^i$ , where  $c_i$  are the  $N$  coefficients of the polynomial.

### 3.2. Signal Propagation

The cosmological 21 cm signal propagated through the SARAS 2 system,  $S(\nu)$ , is related to the input cosmological signal,  $S_0(\nu)$ , by the total efficiency  $\eta_t(\nu)$  of the SARAS 2 monopole antenna; i.e.,  $S(\nu) = \eta_t(\nu) \times S_0(\nu)$ . To model the cosmological component in our data analysis we use 264 different theoretical 21 cm spectra presented by Cohen et al. (2017). In Figure 3 (top) we show a representative set of 25 input cosmological spectra in the 40–200 MHz band, from which the contribution of the CMB has been subtracted. To demonstrate the effect of the SARAS 2 system, in the bottom panel of Figure 3 we show the same signals after they have been propagated through the system. The signals are attenuated when propagated through the system, due to the total efficiency, with the loss increasing toward lower frequencies. The total efficiency of the SARAS 2 system was discussed in Singh et al. (2017b; see Section 3.2.3 and Appendix A). We provide the measured total efficiency in Figure 3 for reference.

### 3.3. Sensitivity Test

In this subsection our goal is to determine the optimal frequency band  $\Delta_{1,2}$ , covering the frequency range  $\nu_1$  to  $\nu_2$ , and the number of polynomial terms,  $N$ , of  $F(\nu)$  that provide the best constraint on the particular signal template,  $S_0(\nu)$ . Using this information in Sections 3.4 and 3.5 we derive the confidence with which each theoretical signal is ruled out by the SARAS 2 data.

We first perform a sensitivity test which, for each one of the 264 input templates  $S_0(\nu)$  and given  $\Delta_{1,2}$  and  $N$ , determines whether or not the signal can in principle be extracted from the data considering the rms thermal noise and the total efficiency of the system  $\eta_t(\nu)$ . The test delineates the 2D  $\Delta_{1,2}$ – $N$  parameter space in which the signal can be either detected or rejected with at least  $1\sigma$  confidence.

For a given  $\Delta_{1,2}$  and  $N$  we first generate 500 independent realizations of mock thermal noise with Gaussian statistics. The rms thermal noise in any mock spectrum is matched to that in the data within the corresponding frequency band. We then add the propagated signal  $S(\nu)$ , in the frequency range  $\nu_1$  to  $\nu_2$ , to each realization of the mock thermal noise, creating 500 mock data sets. Each one of these data sets is then jointly fit with a model using linear least-squares (Press et al. 2007):

$$M(\nu) = F(\nu) + a \times S(\nu), \quad (1)$$

where  $a$  is a scale factor for the signal. The procedure returns best-fit values of the scale factor and coefficients of the polynomial,  $c_i$ , for each mock data set separately. For each realization of the thermal noise, the fitting uncertainties in the polynomial coefficients,  $\sigma_{c_i}$ , and in the scale factor,  $\sigma_a$ , are computed as part of the modeling process from the covariance matrix. We next perform joint fitting for all the 500 data sets and derive the mean,  $\bar{a}$ , and standard deviation,  $\sigma_{\bar{a}}$ , for the scale factor across the ensemble of the mock data sets.

For a detection, the extracted scale factor,  $\bar{a}$ , should be consistent with unity within the fitting uncertainties  $\sigma_{\bar{a}}$ . In other words, for each input signal  $S_0(\nu)$  (and assuming the particular choice of  $\Delta_{1,2}$  and  $N$ ) to be detected with more than  $1\sigma$  confidence; we require the following condition be satisfied:

$$0 < (\bar{a} - \sigma_{\bar{a}}) \leq 1 \leq (\bar{a} + \sigma_{\bar{a}}). \quad (2)$$

If this condition is not satisfied, we infer that the collected data (given its thermal rms noise,  $\Delta_{1,2}$  and  $N$ ) is not sufficient to detect the particular  $S_0(\nu)$  at the  $1\sigma$  level.

This exercise ignores foregrounds and systematics that may leave residuals and this affect the detection of the 21 cm signal. Therefore, it should be considered only as a feasibility test that helps to determine whether or not the rms noise is sufficiently low for a detection with significance greater than  $1\sigma$ . This sensitivity test affirms that if (i) the 21 cm signal is indeed present in the measurement data, and (2) there are no residual foregrounds and systematics limiting the decision, then the best-fit results should yield  $\bar{a} = 1$  with a confidence exceeding  $1\sigma$ .

Examination of the distribution of  $\bar{a}$  for different  $\Delta_{1,2}$  and  $N$  provides a 2D parameter space ( $\Delta_{1,2}$ – $N$ ) in which the condition above is satisfied. We use the allowed values of  $\Delta_{1,2}$  and  $N$  in the next subsection to test each template against real data. If for a particular 21 cm signal the  $\Delta_{1,2}$ – $N$  parameter space is empty, this template is taken out of the ensemble and is not searched for. Therefore, the sensitivity test may be viewed as a

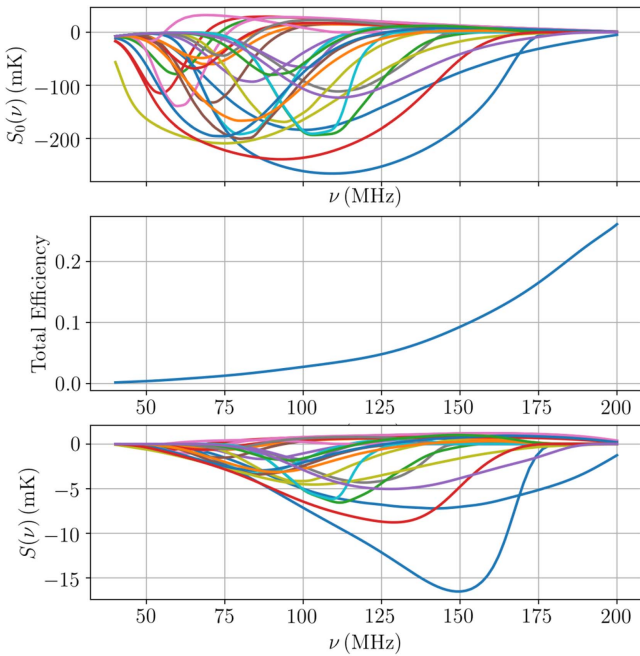


**Figure 3.** Top: representative set of 25 input global 21 cm spectra  $S_0(\nu)$  as a function of frequency in mK units (Cohen et al. 2017). The middle plot shows the total efficiency of the SARAS 2 antenna as computed in Singh et al. (2017b; see Section 3.2.3 and Appendix A). Bottom: propagated spectra,  $S(\nu)$ .

preliminary filter that selects potentially good candidate 21 cm signals that can be detected/rejected using the collected data.

### 3.4. Fitting the Data

We construct a set of models (Equation (1)) for each one of the 21 cm signals that pass the sensitivity test and for every combination of  $\Delta_{1,2}$  and  $N$  from the allowed part of the parameter space. We fit every model to the real data using linear least-squares. The objective function defined as

$$\chi^2 = \sum_{\nu_1}^{\nu_2} w_{\nu_i}^2 (y_{\nu_i} - M(\nu_i))^2 \quad (3)$$

is minimized, where  $y_{\nu_i}$  is the real data in the  $i$ th frequency channel and  $M(\nu_i)$  is the model (Equation (1)).  $w_{\nu_i}$  are the relative weights for the data in each frequency channel  $i$  based on the system temperature and effective integration times, which differ across the band depending on the RFI excision during the processing. The calibrated data, along with the corresponding relative weights across the band, are shown in Figure 4.

In the fitting procedure to the SARAS 2 data, for each given theoretical 21 cm signal that passes the sensitivity test, the optimal  $\Delta_{1,2}$  and  $N$  are selected to be the combination for which the fit yields minimum uncertainty in the scale factor. The best-fit scale factor is denoted as  $\tilde{a}$ , with the standard deviation  $\sigma_{\tilde{a}}$  given by the relevant diagonal term in the corresponding covariance matrix. In our analysis of all the plausible theoretical 21 cm signals in the atlas, the median value of the optimal  $N$  is 4, and the associated frequency band is 110–180 MHz. This is consistent with the fact that the foregrounds and internal systematics of SARAS 2 are indeed spectrally smooth and hence require only low-order polynomials for the modeling. Typically, larger  $N$  remove a greater part of the 21 cm signal and therefore return a larger

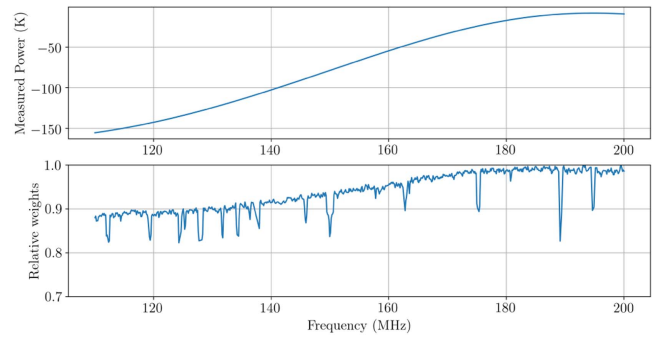


**Figure 4.** Top panel: calibrated data, without correcting for the antenna transfer function. Bottom panel: relative weights for the data in the frequency channels.

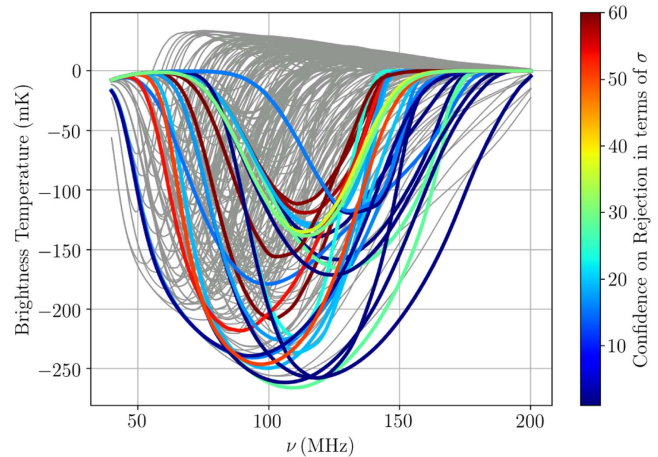


**Figure 5.** The entire set of 264 theoretical models (Cohen et al. 2017). The rejected signals are shown in color, with each color corresponding to the rejection significance as indicated by the color bar. The data do not have sensitivity for the signals shown in gray. Linear least-squares was used to model the foregrounds+systematics.

uncertainty  $\sigma_{\tilde{a}}$ ; while smaller  $N$  are not sufficient to fit the foreground, thus leaving behind larger residuals and increasing the uncertainty  $\sigma_{\tilde{a}}$ .

For each valid theoretical 21 cm signal we compute a standard score,  $\zeta$ , given by

$$\zeta = \left| \frac{1 - \tilde{a}}{\sigma_{\tilde{a}}} \right|. \quad (4)$$

The value of  $\zeta$  yields the confidence of the rejection in units of  $\sigma_{\tilde{a}}$ . Based on this score we rule out any 21 cm signal with  $\zeta > 1$ , which ensures that the signal is inconsistent with the data at greater than the  $1\sigma$  confidence level.

For none of the considered theoretical models was  $\tilde{a}$  found to be consistent with unity, which would indicate a detection. However, we find that for all the theoretical 21 cm signals that pass the sensitivity test, the condition for rejection is satisfied with confidence above  $1\sigma$ ; 25 templates have greater than  $5\sigma$  rejection significance. These cases are shown in color in Figure 5, with each color representing the significance of rejection according to the color bar. The corresponding rejection residuals are shown in the bottom panel of Figure 6. Both the number of rejected cases and the significance of rejection are an improvement compared to our previous work (Singh et al. 2017a). We note that very high values of rejection significance should be interpreted cautiously, since the real data

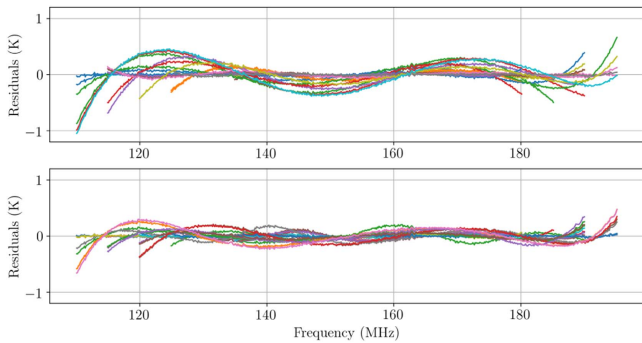


**Figure 6.** Residual obtained after subtracting the fit model from the data, with the band and number of polynomial terms chosen based on the minimum error on the scale factor. Different colors represent residuals for different rejected 21 cm templates. The fitting was performed using nonlinear least-squares for computing the residuals for the top panel, while the residuals in the bottom panel were obtained using linear least-squares.

may include significant systematic noise with substantial non-Gaussianity.

### 3.5. An Alternative Method of Model Fitting Using Nonlinear Optimization

The process of performing the sensitivity test and fitting the data in Sections 3.3 and 3.4, respectively, employ linear least-squares where the best-fit scale factor,  $\bar{a}$ , is unconstrained in the process of modeling. Such an approach may lead to unphysical values of the scale factor.

In order to perform a constrained joint optimization of the scale factor with the polynomial terms, we compute the coefficients and their associated uncertainties using the Levenberg–Marquardt algorithm (Marquardt 1963) for the sensitivity test and fitting the data. Except for the method of optimization, the frameworks for the sensitivity test and data fitting remain the same, where the model is described by Equation (1) and the objective function to be minimized is given by Equation (3).

Nonlinear optimization routines are often biased by the initial guess on the parameters to be estimated; therefore, in the case of the sensitivity test described in Section 3.3, since we are testing for a detection, we provide an initial guess of 0 to the parameter  $\bar{a}$ . Conversely, in the case of modeling the real data, where we are seeking to identify the 21 cm signals that may be ruled out, we provide an initial guess of unity for  $\bar{a}$ . Thus, by providing initial guesses that are the opposite of the outcomes being examined for, we conservatively minimize the chances of a false rejection of 21 cm signals in the fitting to the data. Furthermore, for the given signal, we disallow scale factors less than 0, which would then correspond to a different, inverted signal.

The median value of the optimal  $N$  and the associated frequency band with this approach continue to be the same as that obtained through the linear least-squares approach.

Since this is a constrained nonlinear approach to computing the scale factor, we take a more conservative approach in rejecting the signal. We rule out any 21 cm signal for which the following condition is met:

$$(\bar{a} - \sigma_{\bar{a}}) \leq 0 \leq (\bar{a} + \sigma_{\bar{a}}) < 1. \quad (5)$$

While  $(\bar{a} + \sigma_{\bar{a}}) < 1$  ensures that the signal is inconsistent with the data with greater than  $1\sigma$  confidence, the condition  $(\bar{a} - \sigma_{\bar{a}}) \leq 0 \leq (\bar{a} + \sigma_{\bar{a}})$  ensures that the best-fit scale factor

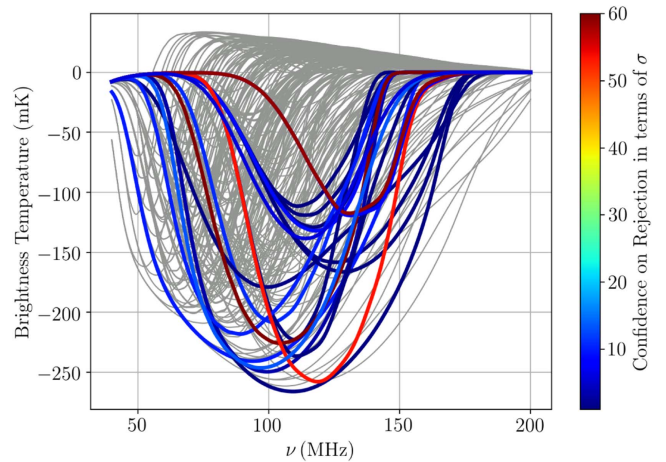


**Figure 7.** The entire set of 264 theoretical models (Cohen et al. 2017). The rejected signals are shown in color, with each color corresponding to the rejection significance as indicated by the color bar. The data do not have sensitivity for the signals shown in gray. Nonlinear optimization was used to model the foregrounds+systematics.

is consistent with 0 within  $\pm 1\sigma$ . The value of  $\zeta$ , as defined in Equation (4), yields the confidence of the rejection in units of  $\sigma$ .

Using the method of nonlinear optimization and the same set of theoretical models of global 21 cm signals, we reject 20 templates with significance of rejection exceeding  $1\sigma$ . The rejected templates form the subset of models ruled out using linear least-squares criteria. We highlight the rejected models in Figure 7, where the color denotes the significance of rejection in units of  $\sigma$ . The corresponding data residuals are shown in the top panel of Figure 6. We next proceed to investigate the parameter space spanned by the 20 rejected templates.

## 4. SARAS 2 Constraints on 21 cm from CD/EoR

In the parameter study conducted by Cohen et al. (2017), the entire astrophysical parameter space allowed by current observational and theoretical constraints was sampled, and the 21 cm signals were derived for different combinations of the astrophysical parameters. In this study, key astrophysical parameters were varied, including the minimal circular velocity of star-forming halos (starting from the minimal velocity of  $4.2 \text{ km s}^{-1}$  characteristic for star formation via molecular cooling and up to  $76.5 \text{ km s}^{-1}$ ), star formation efficiency (SFE) between 0.5% and 50%, spectral energy distribution (SED) of X-ray sources including hard and soft spectra (Fialkov et al. 2014), X-ray efficiency compared to the low-redshift counterparts, mean free path (mfp) of ionizing radiation (cases with 5, 20, and 70 Mpc were considered), and the total optical depth,  $\tau$ . The data collected by SARAS 2 is sufficient to rule out 8% of the considered theoretical models.

The rejected models all share similar astrophysical properties: rapid reionization in tandem with either late X-ray heating due to very inefficient sources (10 cases) or no heating at all (10 cases). In all these models the gas does not have enough time to heat up to the temperature of the CMB, and the 21 cm signal is seen in absorption throughout the EoR (colored lines in Figure 7).

All the models ruled out by the SARAS 2 data share rapid reionization. We quantify this by the maximum rate of change

**Table 1**  
Parameters of the 21 cm Signals Rejected by the SARAS 2 Data

$f^*$	$V_c$ (km s $^{-1}$ )	$f_X$	SED	$\tau$	$R_{\text{mfp}}$	$\left(\frac{dS_0}{dz}\right)_{\text{max}}$	Band (MHz)	Number of Polynomial Terms (N)	Significance of Rejection
0.005	35.50	0	Hard	0.082	20	67.40	110–195	4	1.26
0.005	35.50	1	Hard	0.082	70	69.71	110–190	4	1.40
0.050	16.50	0	Hard	0.096	70	94.92	115–180	4	1.89
0.005	35.50	0.1	Soft	0.082	70	88.33	110–185	4	3.23
0.500	35.50	0	Hard	0.082	20	94.45	120–195	4	4.88
0.500	76.50	0.1	Hard	0.066	70	97.17	125–190	4	5.63
0.005	4.20	0	Hard	0.082	70	74.32	135–190	4	8.01
0.500	76.50	0.1	Hard	0.082	70	128.98	110–195	5	8.27
0.050	35.50	0.1	Hard	0.082	70	94.26	115–190	4	8.90
0.005	35.50	0.1	Hard	0.082	70	110.48	125–180	4	9.84
0.500	4.20	0	Hard	0.082	70	164.83	135–180	4	10.06
0.005	35.50	0.1	Hard	0.066	70	104.18	110–190	5	10.83
0.015	76.50	0.1	MQ	0.066	70	146.62	125–195	6	12.41
0.005	35.50	0	Hard	0.082	70	118.34	110–180	5	13.31
0.015	76.50	0.1	Soft	0.066	70	159.21	115–195	6	16.40
0.050	35.50	0	Hard	0.083	70	164.71	115–180	6	18.56
0.500	76.50	0.1	MQ	0.066	70	169.85	115–190	6	31.24
0.500	35.50	0	Hard	0.082	70	172.80	115–175	6	53.42
0.005	35.50	0	Hard	0.066	70	131.70	115–180	5	58.94
0.500	35.50	0	Hard	0.066	70	172.59	115–195	8	89.20

**Note.**  $f^*$  denotes the star formation efficiency,  $V_c$  represents minimum virial circular velocity for star formation,  $f_X$  is the efficiency of the X-ray sources, SED refers to the spectral energy distribution of X-ray sources. The SEDs considered are of hard and soft X-ray sources, along with that of mini-quasars (MQ).  $\tau$  is CMB optical depth,  $R_{\text{mfp}}$  denotes the mean free path of ionizing photons, and  $\left(\frac{dS_0}{dz}\right)_{\text{max}}$  is the maximum rate of change of the brightness temperature of the signal with respect to redshift. The significance of rejection is computed as given in Equation (4). A detailed description of most of these parameters is given in Cohen et al. (2017).

of the brightness temperature of the 21 cm signal with respect to redshift,  $\left(\frac{dS_0}{dz}\right)_{\text{max}}$ . The rejected signals have high values of  $\left(\frac{dS_0}{dz}\right)_{\text{max}}$ , with the median value of the rejected set being 114 mK over the  $z \sim 10$ –6 redshift interval. This is in contrast to the set of non-rejected signals where the median value of  $\left(\frac{dS_0}{dz}\right)_{\text{max}}$  is 9 mK over the same redshift range. Rapid reionization scenarios typically require one or more of the following: a large mfp of the ionizing photons, high star formation, and ionizing efficiencies of the sources. All but two rejected cases have an mfp of 70 Mpc; however, the values of SFE and  $\tau$  are unconstrained. The other 2 cases have mfps of 20 Mpc and high values of  $\tau$ . None of the rejected cases have an mfp of 5 Mpc.

Considering “inefficient heating” models (sources with X-ray bolometric luminosity per star formation rate of up to 10% of their low-redshift counterparts) all the rejected cases share late star formation, which only happens in massive halos with circular velocities above 35 km s $^{-1}$ . In these cases, the absorption trough is shifted into the SARAS 2 band, owing to the delayed build up of the Ly $\alpha$  background, making either detection or rejection easier. The majority of these cases have hard X-ray SEDs, while the value of SFE varies from model to model.

The rejected astrophysical models with “no heating” have all possible values of circular velocities (from 4.2 to 76.5 km s $^{-1}$ ), SFE (from 0.5% to 50%) and values of  $\tau$ . Out of the 264 tested models, the only cases with “no heating” that were not ruled out have either very efficient star formation in light halos, and thus the absorption peak is shifted out of the SARAS 2 band, or have short mfp (5 Mpc), which implies more gradual reionization.

A summary of astrophysical parameters for the rejected signals, along with the optimal band, number of polynomial terms, and significance of rejection, is listed in Table 1.

## 5. Caveats

Experiments aiming to detect the global 21 cm from CD/EoR are difficult long-wavelength radiometer measurements, and require a substantially wider dynamic range than what is typically necessary in most engineering applications at these frequencies. Limitations may arise from unknowns in the internal systematics, antenna characteristics, ground emission, low-level distributed RFI, and mode-coupling of sky spatial structure into spectral measurement data owing to frequency-dependent beams.

If the measurement equation describes the data to mK levels, including foregrounds and internal systematics, then a forward-modeling approach is expected to be unbiased. This would apply even in the case of an excessive modeling of foreground+systematics with a higher than necessary order polynomial (which, however, would degrade the confidence in the derived results). In an extreme case, if the model adopted for the foreground+systematics is also capable of fitting out the 21 cm template, the result would be completely ambiguous, with equal likelihoods for the presence and absence of the template.

Problems potentially arise when the measurement equation or the adopted model is inadequate to describe the foreground+systematics, given the large dynamic range required for 21 cm signal detection. In this case, residual systematics can bias the results of the decision tests. The adoption of an inadequate model may be inadvertent, particularly in the case where 21 cm signals are extracted via statistical analysis that aims to detect the signals in measurement data wherein the signal-to-noise ratio in individual channels are substantially below unity.

Adopting an inadequate model would result in systematic residuals to the fit to foregrounds+systematics. The least-squares fit would attempt to maximize the correlation (or anti-correlation) of these residuals to the 21 cm template under consideration so that including a scale factor times the 21 cm template, the overall residuals would be a minimum. Consequently, the unmodeled foreground+systematics might partially or wholly mimic the 21 cm signal—thus yielding a false positive—or partially or wholly cancel a true 21 cm signal in the data, thus yielding a false negative. In these circumstances small fit residuals might suggest excellent fits with low formal statistical errors in the fitted scale factor  $a$ ; however, the errors are obviously underestimates, since the unmodeled systematics are not considered in the error computation.

It is also necessary to consider cases where the true cosmological signal in the measurement data is substantially different from the template used in modeling. If the true cosmological signal is uncorrelated with the template, then the fit value of the scale factor  $a$  will not be biased. However, if there is partial correlation (or anti-correlation), then the fit would bias the  $a$  parameter to be positive or negative depending on the correlation or anti-correlation, respectively.

The work presented herein has adopted polynomial models for the foreground+systematics. A higher  $N$  would obviously fit this term better; however, it would also increasingly subsume the cosmological signal and hence reduce the confidence in either detection or rejection. Future effort should be directed toward improve the modeling of foregrounds +systematics and should avoid fitting out of a significant fraction of 21 cm signals. The design of SARAS 2, which aims to constrain the systematics to be maximally smooth (Singh et al. 2018), follows that line of approach.

## 6. Conclusion


In this work we have analyzed the first-light data from SARAS 2 using a frequentist approach and forward-modeling. The revised analysis has led to the rejection of 20 plausible 21cm signals out of 264 tested models. In 15 cases, the confidence of the rejection is above  $5\sigma$ . All the rejected signals lie in the regime of either late or non-existent heating by the first population of X-ray sources, which creates a deep absorption trough in the 21 cm signal observed against the CMB. In addition, in all the rejected models, reionization happens fast owing to the assumed long mfp of the ionizing photons, as well as efficient star formation and ionization. We leave robust estimation of the rejected parameter space to future work.

We thank the staff at Gauribidanur Field Station for assistance with system tests and measurements, and the Mechanical and Electronics Engineering Groups at Raman Research Institute for building and assembling SARAS 2.

Santosh Harish and Divya Jayasankar implemented real-time software and monitoring. Logistics and technical support for observations was provided by Indian Astronomical Observatory, Leh operated by Indian Institute of Astrophysics, and Timbaktu Collective, India. For R.B. and A.C. this project/publication was made possible through the support of a grant from the John Templeton Foundation. The opinions expressed in this publication are those of the author(s) and do not necessarily reflect the views of the John Templeton Foundation. This research was also supported (for R.B. and A.C.) by the ISF-NSFC joint research program (grant No. 2580/17).

## ORCID iDs

Saurabh Singh  <https://orcid.org/0000-0001-7755-902X>

Ravi Subrahmanyam  <https://orcid.org/0000-0001-9913-900X>

Anastasia Fialkov  <https://orcid.org/0000-0002-1369-633X>

A. Raghunathan  <https://orcid.org/0000-0003-1929-9869>

## References

- Barkana, R. 2016, *PhR*, **645**, 1
- Bernardi, G., Zwart, J. T. L., Price, D., et al. 2016, *MNRAS*, **461**, 2847
- Bowman, J. D., & Rogers, A. E. E. 2010, *Natur*, **468**, 796
- Cohen, A., Fialkov, A., Barkana, R., & Lotem, M. 2017, *MNRAS*, **472**, 1915
- Evoli, C., Mesinger, A., & Ferrara, A. 2014, *JCAP*, **11**, 024
- Fialkov, A., & Barkana, R. 2014, *MNRAS*, **445**, 213
- Fialkov, A., Barkana, R., & Visbal, E. 2014, *Natur*, **506**, 197
- Fialkov, A., & Loeb, A. 2016, *ApJ*, **821**, 59
- Field, G. B. 1958, *PIRE*, **46**, 240
- Furlanetto, S. R. 2006, *MNRAS*, **371**, 867
- Liu, A., Pritchard, J. R., Allison, R., et al. 2016, *PhRvD*, **93**, 043013
- Marquardt, D. W. 1963, *SIAM Journal on Applied Mathematics*, **11**, 431
- Mirocha, J., Harker, G. J. A., & Burns, J. O. 2013, *ApJ*, **777**, 118
- Mirocha, J., Harker, G. J. A., & Burns, J. O. 2015, *ApJ*, **813**, 11
- Mirocha, J., Mebane, R. H., Furlanetto, S. R., Singal, K., & Trinh, D. 2017, arXiv:1710.02530
- Monsalve, R. A., Rogers, A. E. E., Bowman, J. D., & Mozden, T. J. 2017, *ApJ*, **847**, 64
- Oppenheim, A. 1999, *Discrete-Time Signal Processing* (India: Pearson Education)
- Press, W. H., Teukolsky, S. A., Vetterling, W. T., & Flannery, B. P. 2007, *Numerical Recipes 3rd Edition: The Art of Scientific Computing*, 3rd edn. (New York: Cambridge Univ. Press)
- Pritchard, J. R., & Loeb, A. 2010, *PhRvD*, **82**, 023006
- Sathyanarayana Rao, M., Subrahmanyam, R., Udaya Shankar, N., & Chluba, J. 2017a, *AJ*, **153**, 26
- Sathyanarayana Rao, M., Subrahmanyam, R., Udaya Shankar, N., & Chluba, J. 2017b, *ApJ*, **840**, 33
- Shaver, P. A., Windhorst, R. A., Madau, P., & de Bruyn, A. G. 1999, *A&A*, **345**, 380
- Singh, S., Subrahmanyam, R., Shankar, N. U., et al. 2017, *ApJL*, **845**, L12
- Singh, S., Subrahmanyam, R., Shankar, N. U., et al. 2018, *ExA*, **45**, 269
- Sitwell, M., Mesinger, A., Ma, Y.-Z., & Sigurdson, K. 2014, *MNRAS*, **438**, 2664
- Visbal, E., Barkana, R., Fialkov, A., Tseliakhovich, D., & Hirata, C. M. 2012, *Natur*, **487**, 70
- Wouthuysen, S. A. 1952, *AJ*, **57**, 31